

Tailoring mechanically-tunable strain fields in graphene

M. Goldsche,^{1,2,*} J. Sonntag,^{1,2,*} T. Khodkov,^{1,2} G. Verbiest,¹ S. Reichardt,^{1,3}
C. Neumann,^{1,2} T. Ouaj,¹ N. von den Driesch,² D. Buca,² and C. Stampfer^{1,2}

¹*JARA-FIT and 2nd Institute of Physics, RWTH Aachen University, 52056 Aachen, Germany, EU*

²*Peter Grünberg Institute (PGI-8/9), Forschungszentrum Jülich, 52425 Jülich, Germany, EU*

³*Physics and Materials Science Research Unit, University of Luxembourg, 1511 Luxembourg, Luxembourg, EU*

There are a number of theoretical proposals based on strain engineering of graphene and other two-dimensional materials, however purely mechanical control of strain fields in these systems has remained a major challenge. The two approaches mostly used so far either couple the electrical and mechanical properties of the system simultaneously or introduce some unwanted disturbances due to the substrate. Here, we report on silicon micro-machined comb-drive actuators to controllably and reproducibly induce strain in a suspended graphene sheet, in an entirely mechanical way. We use spatially resolved confocal Raman spectroscopy to quantify the induced strain, and we show that different strain fields can be obtained by engineering the clamping geometry, including tunable strain gradients of up to 1.4 %/ μm . Our approach also allows for multiple axis straining and is equally applicable to other two-dimensional materials, opening the door to an investigating their mechanical and electromechanical properties. Our measurements also clearly identify defects at the edges of a graphene sheet as being weak spots responsible for its mechanical failure.

Keywords: Graphene, MEMS, Raman spectroscopy, strain engineering, pseudomagnetic field

Applying strain fields in graphene not only allows tailoring its mechanical properties¹, but also reveals fascinating phenomena such as pseudomagnetic fields²⁻⁴, valley filters^{5,6}, superconductivity⁷, or pseudo gravitomagnetic forces⁸. Although these phenomena have received much attention theoretically, controlling the required strain fields and strain gradients has remained a major challenge. Here we present micro-machined comb-drive actuators with integrated graphene for engineering truly mechanically-tunable strain fields. We use spatially resolved confocal Raman spectroscopy⁹ to quantify the strain fields as a function of a controllably induced displacement. Different strain fields can be obtained by engineering the clamping geometry, including tunable strain gradients up to 1.4 %/ μm . The presented approach also allows for multiple axis straining and is applicable to the rising number of other two-dimensional materials, thus providing a workhorse for investigating the fundamental electromechanical properties of 2D materials as well as for developing new sensor and transducer concepts.

Strain is commonly induced in graphene by pulling on suspended sheets with an electrostatic gate^{1,10-14} or by bending a flexible substrate^{5,6,9,12,13}. The obtained strain fields are thus intrinsically linked to either the electronic tuning of the charge carrier density or to the properties of the substrate. This lack of independent control over strain fields poses a great challenge for any application based on strain engineered graphene. Moreover, engineering truly controllable local strain patterns in graphene has not been achieved so far. Our comb-drive (CD) actuators give independent control and allow for engineered strain fields.

The CD actuators with integrated graphene (schematic

in Figure 1a) are based on surface micro-machining of silicon-on-insulator substrates and on transferring mechanically exfoliated graphene flakes. Crucially, we use a polymethylmethacrylate (PMMA) membrane to place the graphene flake onto the CD devices, which is then used to clamp the graphene flake by locally cross-linking it. After dissolving the remaining PMMA, we use hydrofluoric acid to suspend the complete device (see Methods and Supplementary Figure 1). Figure 1b shows a false color scanning electron microscope (SEM) image of such a device. The actuator consists of a suspended body that is connected by four springs to fixed anchors. The suspended body has multiple interdigitated fingers with a fixed body (Figure 1c and d). A potential difference V_a between the fingers gives rise to an electrostatic force $F = \eta V_a^2$ (Figure 1c), where 2η is the capacitive coupling¹⁸. Our devices controllably reach a maximum displacement of 60 nm, which translates into $\sim 6\%$ of strain in the suspended part of the graphene flake (Supplementary Figure 3).

To monitor strain and to map spatially resolved strain fields, we use scanning confocal Raman microscopy (see Methods and Supplementary Figure 4). Typical Raman spectra featuring the prominent Raman G and 2D peaks are shown in Figure 1e and f, respectively. We usually do not observe a D peak on the suspended part of the investigated graphene sheets. The force F applied to the suspended graphene flake results in a red shift of the G and 2D peak with increasing $|V_a|$ due to strain. As the CD design allows the application of purely uniaxial strain, we observe a splitting of the G peak for high strain values (arrows in Figure 1e), in good agreement with Mohiuddin et al.⁵, which proves the strength of the CD actuators. The splitting allows us to extract a Pois-

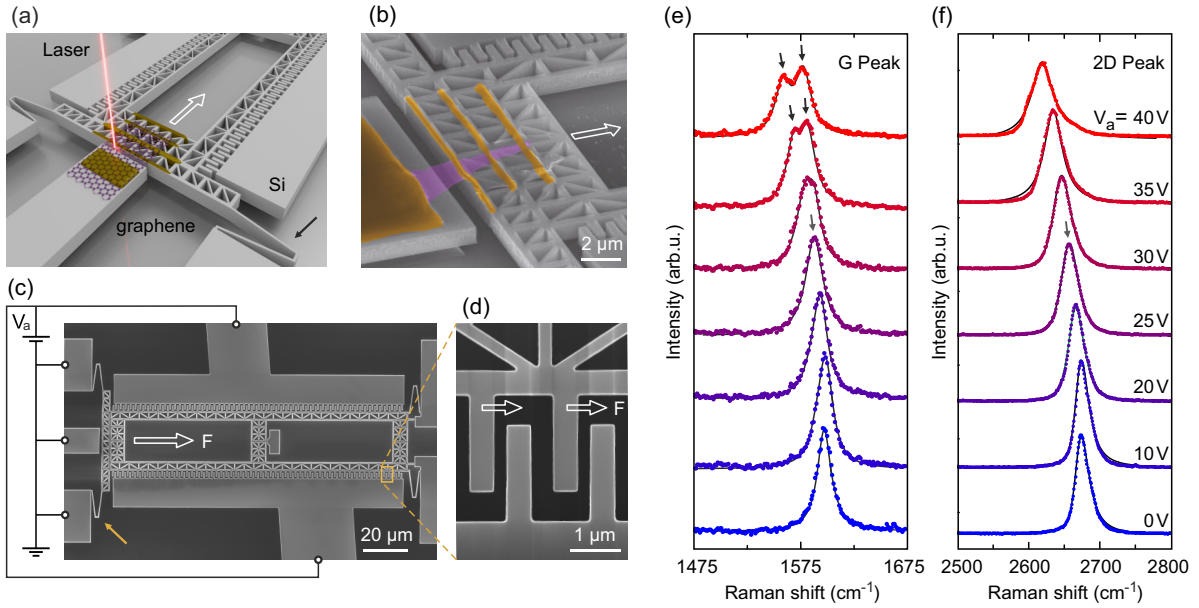


Figure 1. (a) Schematic illustration of a comb-drive (CD) actuator that applies uniaxial strain to the graphene flake by moving into the direction of the white arrow. (b) False color scanning electron microscope (SEM) image of a measured device, in which the cross-linked PMMA clamping (yellow) of the graphene (pink) is highlighted. (c) Top view SEM image of a fabricated CD actuator. The applied potential V_a generates an electrostatic force F between the interdigitated fingers of the fixed and the suspended part of the CD actuator. The fixed part is resting on the substrate whereas the suspended part is freely hanging and is held by four V-shaped springs (see yellow arrow). (d) Close-up showing the asymmetric distance between the fingers to ensure movement of the suspended part in the direction indicated by the arrow alongside F . (e) The Raman spectrum of the G peak for increasing V_a shows a red shift and a splitting into two peaks due to strain. (f) The Raman spectrum of the 2D peak only shows a red shift with increasing V_a . The black lines in panels (e) and (f) are fits to Lorentzian peaks that are used to extract ω_G and ω_{2D} , respectively.

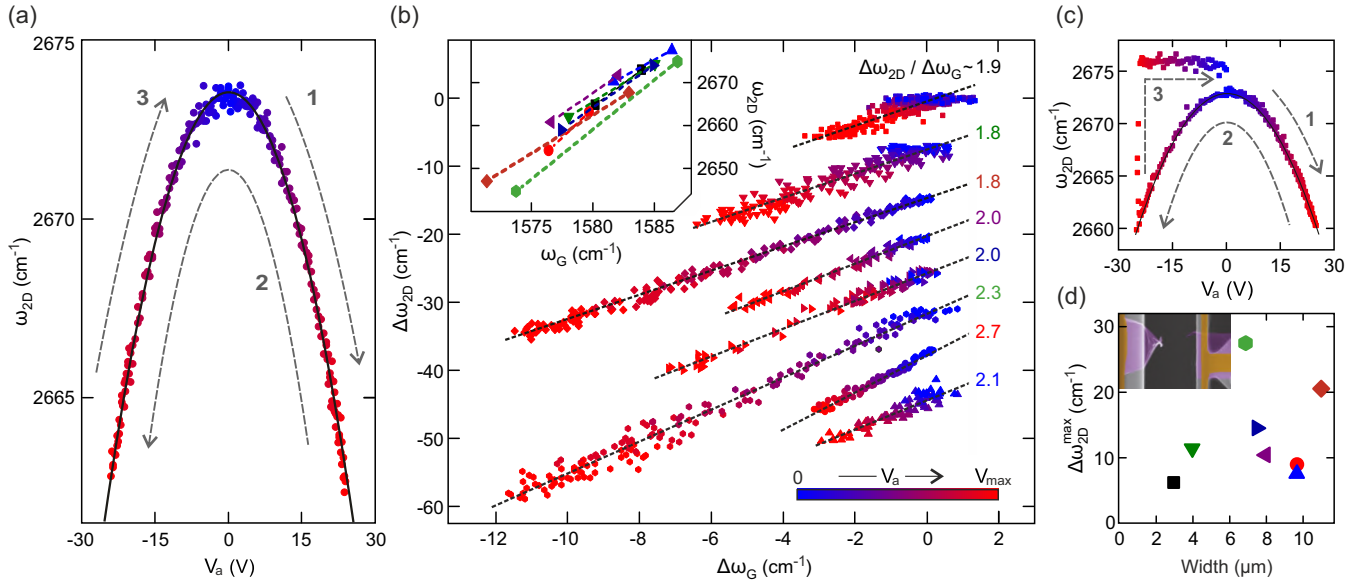


Figure 2. (a) ω_{2D} versus V_a shows parabolic behavior. The grey arrows 1 to 3 indicate the sweep direction of the potential V_a in the measurement. (b) $\Delta\omega_{2D}$ versus $\Delta\omega_G$ shows a linear dependence. Each curve is offset for clarity by $\Delta\omega_{2D} = 5 \text{ cm}^{-1}$. The slope $\Delta\omega_{2D}/\Delta\omega_G$ determined from eight different samples is on average 2.1. The inset shows the absolute frequencies ω_{2D} and ω_G as reference. (c) We observe the rupturing of the flake as a jump in ω_{2D} when the potential V_a is swept. The frequency ω_{2D} typically jumps to a value above the one initially measured. (d) The maximum shift $\Delta\omega_{2D}^{\max}$ at which the graphene flake ruptures shows no correlation with the width of the flake. A false colored SEM image (similar to Figure 1b) of a ruptured graphene sheet (see inset) confirms the tearing at the edges. Each different sample has a unique color and symbol in panels (b) and (d).

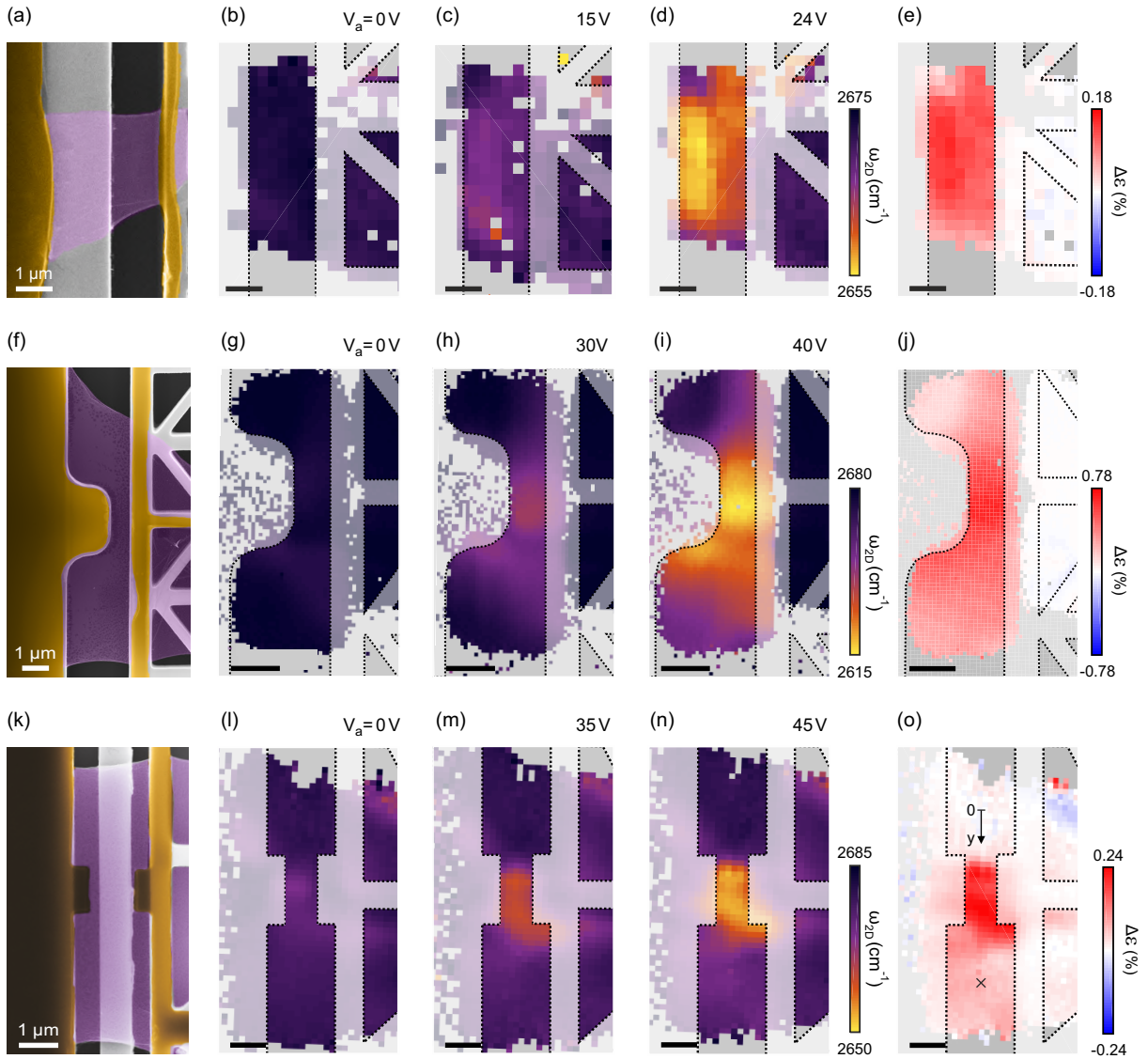


Figure 3. (a) False color SEM image (similar to Figure 1b) of a typically measured device without noses. (b)-(d) Spatially resolved Raman maps of ω_{2D} for increasing V_a : (b) $V_a = 0$ V, (c) $V_a = 15$ V, and (d) $V_a = 24$ V. Note that these are taken on a different sample than the one shown in panel (a). (e) The spatially resolved relative strain $\Delta\epsilon$ at $V_a = 24$ V. (f)-(j) Similar as panels (a)-(e) for the CD design with a silicon nose. Please note the different V_a values. (k)-(o) Similar as panels (a)-(e) for the CD design where the PMMA-clamping contains two noses. The CD design with the noses generate a strain hotspot at the position where the suspended length of the graphene is smallest. All black scale bars correspond to 1 μm .

son ratio of $\nu = 0.11$ (Supplementary Figure 5), which is in good agreement with the one reported in the literature for graphite and suspended graphene⁵.

In the following, we focus on the low strain regime where both the G and 2D peak can be fitted by a single Lorentzian with center frequencies ω_G and ω_{2D} , respectively. When sweeping V_a back and forth many times (Figure 2a and Supplementary Figure 6 and 7), we observe no hysteresis and hence no noticeable slipping of the clamped graphene. The actuator thus induces strain in a controllable and reproducible fashion. The center frequencies as a function of V_a show a clear parabolic dependence (Figure 2a) reflecting the linear stress-strain

relation

$$\Delta\omega_{2D} = \frac{\partial\omega_{2D}}{\partial\epsilon}\Delta\epsilon = \frac{\partial\omega_{2D}}{\partial\epsilon} \frac{F}{k'L} = \frac{\partial\omega_{2D}}{\partial\epsilon} \frac{\eta V_a^2}{k'L}, \quad (1)$$

where $\Delta\omega_{2D}$ is the shift in center frequency ω_{2D} ($\Delta\omega_G$ is analogue), $\partial\omega_{2D}/\partial\epsilon = -83 \text{ cm}^{-1}/\%$ describes the relative ω_{2D} shift per unit strain ϵ (Supplementary Table 1), $\Delta\epsilon$ is the induced strain, and k' a combined spring constant, which takes into account the graphene flake suspended over the length L , the clamping and the actuator (Supplementary Discussion 1 and Supplementary Figures 8-10).

The shift in center frequencies are determined by the Grüneisen parameters of both phonon modes⁵. These

Grüneisen parameters quantify the anharmonicity of the lattice with respect to the direction of applied strain. Consequently, the Grüneisen parameters¹⁹ are (slightly) dependent on the crystallographic orientation, which is seen in Figure 2b as a variation in slopes between $\Delta\omega_{2D}$ and $\Delta\omega_G$ for eight different devices. The slope equals the ratio of the Grüneisen parameters^{5,19} and we observe values ranging from 1.9 to 2.7 (see labels in Figure 2b). This agrees with the values between 1.9 and 3 reported in the literature¹⁹.

The maximum relative shift of ω_{2D} before mechanical failure is around 30 cm^{-1} , which corresponds to at most 0.4% of strain (inset Figure 2b). Figure 2c shows a typical example of a mechanical failure. This particular graphene sheet teared while approaching $V_a = -24 \text{ V}$. This releases all strain, which results in a sudden hardening of ω_{2D} , which jumps to values above the one at $V_a = 0 \text{ V}$, due to the release of the existing pre-strain introduced during the fabrication process. SEM-pictures of broken devices (see e.g. the inset of Figure 2d) confirm that the suspended graphene flake ruptured. This implies that the PMMA-based clamping technique does not limit the maximum amount of strain that our samples can withstand. The actuators can induce forces strong enough to rip the suspended graphene apart. The surprisingly low rupturing point of the graphene flake (Figure 2d) seems to be in contradiction with literature^{20,21}.

To resolve strain patterns and to see where the graphene sheet ruptures, we use spatially resolved Raman spectroscopy. The graphene sheet in Figure 3a shows a uniform red shift of ω_{2D} with increasing V_a , due to strain (Figure 3b-d). The relative shift of ω_{2D} (Figure 3e) illustrates the presence of strain at the edges. Defects at the edges likely act as starting points for cracks propagating through the graphene flake when the overall strain is still low ($\sim 0.3\%$) causing the mechanical failure.

To reduce the strain at the edges and to get control over the strain field in the bulk of the suspended graphene flake, we modify the clamping geometry. Here, we employed two different methods: (i) the CD actuator is designed with a nose and (ii) the pattern of the cross-linked PMMA includes two noses. The noses locally reduce the distance between the fixed anchor and the suspended body of the CD actuator, which results in a higher strain in relation to the strain at the edge. Typical results for methods (i) and (ii) are shown in Figure 3f-j and Figure 3k-o, respectively. Both methods show strain hotspots located at positions where the distance between the fixed anchor and the suspended body is minimal. The strain in the hotspots is up to 4 times larger than at the edges. Note the presence of a strain hotspot at $V_a = 0 \text{ V}$ for method (ii). We reached a maximum strain of 1.2% in the hotspots, which largely exceeds the rupturing strain of 0.3% for the devices shown in Figure 2d. This not only highlights the crucial role of clamping in translating the applied force to strain, but also reinforces the conclusion that the edges are responsible for the low rupturing point.

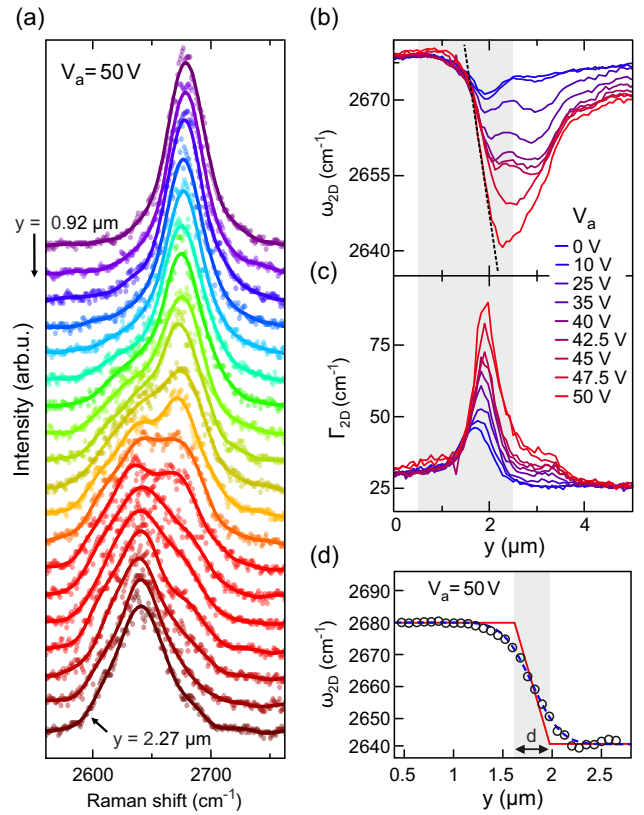


Figure 4. (a) Raman spectrum around the 2D peak along the y -direction highlighted in Figure 3o (at $V_a = 50 \text{ V}$). (b) ω_{2D} along the y -direction as shown in Figure 3o (see cross for end point) for different applied potentials V_a . The black dashed line indicates the maximum strain gradient. (c) Γ_{2D} shows a strong inhomogeneous broadening at the positions where the strain gradient in panel (b) is maximum. (d) To quantify the strain gradient in the grey shaded area in panels (b) and (c), we convolute a piecewise linear function with width d (arrow) with the laser spot. The fit result gives us a width d of 325 nm, which corresponds to a gradient $\partial\omega_{2D}/\partial y = 117 \text{ cm}^{-1}/\mu\text{m}$ or $\partial\epsilon/\partial y = 1.4 \text{ \%/}\mu\text{m}$ at $V_a = 50 \text{ V}$.

The control over strain fields also allows to design and control strain *gradients*. Figure 4a shows that the 2D peak frequency decreases when scanning over the strain gradient in the y -direction of highest strain (see line in Figure 3o). This frequency shift is shown in Figure 4b as a function of position. The highest strain gradients are on the left flank of the hotspot (Figure 4b), which corresponds to the upper edge of the PMMA-jut in Figure 3o. In the region of highest strain gradient, there is also a clear broadening of the 2D peak, which cannot be associated with a splitting into two sub-peaks⁶, since the widths of the peaks in the regions of high and low strain are similar (Figure 4c). We attribute it instead to inhomogeneous broadening, due to the fact that, in the region of strong strain gradient, the laser spot sample areas with different strain conditions^{22,23}.

Consequently, we have to deconvolve the extracted ω_{2D} (Figure 4a) into a piecewise-linear function of width d

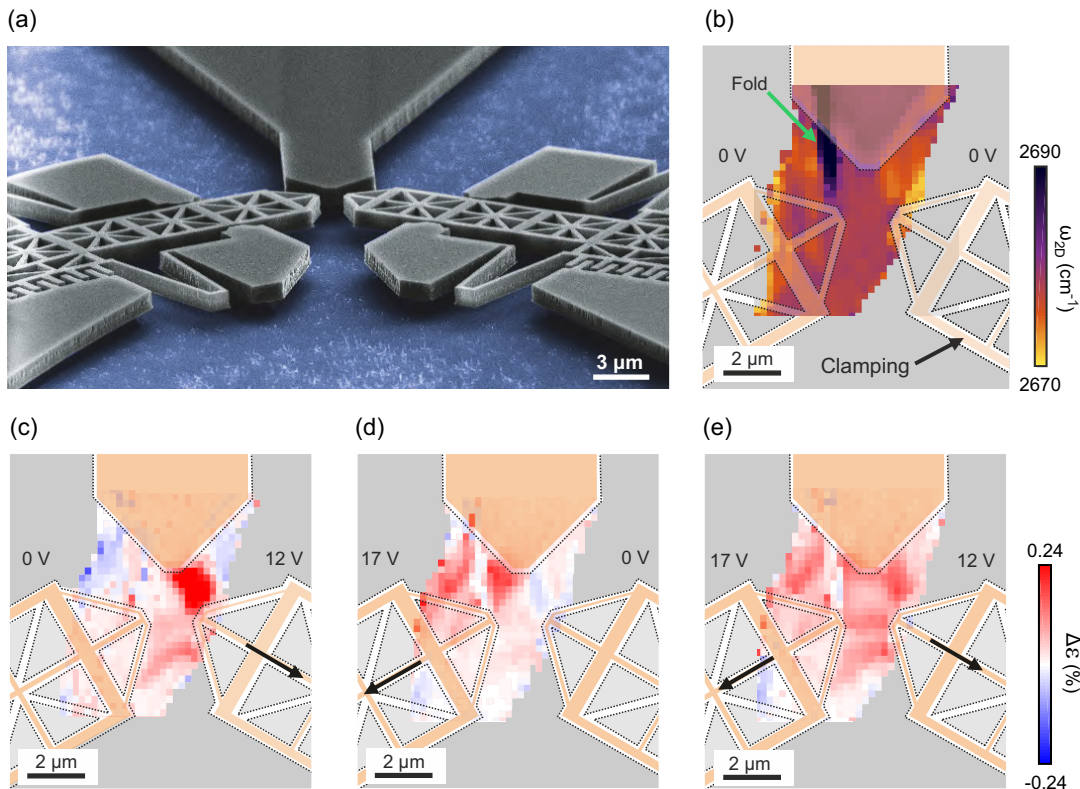


Figure 5. (a) False color SEM image of our fabricated MEMS device with two CD actuators (grey). (b) Spatially resolved Raman map of ω_{2D} for $V_a = 0$ V on both actuators. (c)-(e) The spatially resolved relative strain $\Delta\epsilon$ for increasing V_a : (c) $V_a = 0$ V on the left actuator and $V_a = 12$ V on the right actuator, (d) $V_a = 17$ V on the left actuator and $V_a = 0$ V on the right actuator, and (e) $V_a = 17$ V on the left actuator and $V_a = 12$ V on the right actuator. Note the blue shift of ω_{2D} if 0 V is applied (panels (c) and (d)) to one of the CD actuators, which corresponds to a relative compression of the graphene flake. The cross-linked PMMA areas are shaded orange in panels (b)-(e).

(Figure 4d) and the laser spot, which is modeled by a Gaussian function with a diameter of 505 ± 10 nm (Supplementary Figure 11) to determine the actual strain profile. At $V_a = 50$ V, we find $d = 325$ nm, which corresponds to a gradient of $\partial\omega_{2D}/\partial y = 117$ $\text{cm}^{-1}/\mu\text{m}$ and thus to a strain gradient of $\partial\epsilon/\partial y = 1.4$ $\%/ \mu\text{m}$. Assuming the strain is applied in the armchair direction², a strain gradient of 1.4 $\%/ \mu\text{m}$ induces a pseudomagnetic field of $B_{ps} = \hbar\beta/2ae \cdot \partial\epsilon/\partial y = 120$ mT, where $\beta = 3.37$ is the logarithmic derivative of the nearest-neighbour hopping parameter and $a = 1.42$ \AA is the nearest-neighbour distance. This B_{ps} is strong enough to bring state-of-the-art ultra-clean graphene devices²⁴⁻²⁶ into the quantum Hall regime, which is considered a crucial step for the realization of valley-tronics²⁷.

A very promising geometry for a uniform pseudomagnetic field in graphene requires triaxial strain fields⁴. We realize such strain fields by integrating graphene on two 120° rotated CD actuators placed close to each other (Figure 5a). The ω_{2D} Raman maps in Figure 5b-e show the independent control of the strain in graphene clamped onto the two different CD actuators and the fixed anchor. Interestingly, a single CD actuator not only pulls the graphene sheet but also the other CD actuator, which results in a relative blue shift of the ω_{2D} frequency

and thus locally in compressive strain (Figure 5c and d). By applying approximately equal forces with both CD actuators, we obtain a triaxial strain field in the center region (Figure 5e).

In conclusion our approach allows to induce well controlled and tunable strain fields in two-dimensional materials without any spurious effect due to capacitive coupling to the suspended flake or interaction with the substrate. Understanding and controlling strain in two-dimensional materials will not only advance fundamental knowledge of the unique electromechanical coupling of graphene and other 2D materials, but will also enable ways for dynamically manipulating carriers for novel device applications.

Methods. *Experimental methods and details.* We fabricate the micro-actuators on a silicon on insulator (SOI) substrate following the process described in Ref.²⁸. The substrate consists from bottom to top of a 500 μm thick Si layer, a 1 μm thick SiO_2 layer, and a 2 μm chemical vapor deposited crystalline, highly p-doped silicon layer. The doping of the top layer is 10^{19} cm^{-3} , making our devices low temperature compatible²⁹. The process flow is depicted in Supplementary Figure 1. Using standard electron beam lithography techniques and reactive ion etching with C_4F_8 and SF_6 , we pattern the

CD actuators, shown in Figure 1b and c. The graphene crystals are prepared by mechanical exfoliation from bulk graphite on top of PMMA. Consequently, we transfer the graphene-PMMA stack onto the SOI substrate^{30,31} with an accuracy of $\sim 1 \mu\text{m}$ using micro-manipulators and an optical microscope. Afterwards, the graphene is fixed to the actuator by cross-linking the top PMMA layer at certain locations (see Figure 1b). After dissolving the not cross-linked PMMA with acetone, we suspend the micro-actuator by etching the SiO_2 underneath with 10% hydrofluoric acid solution. Finally, a critical-point drying step is used to prevent the CD actuator from collapsing due to capillary forces.

Raman measurements. We use a partly home-built low temperature ($\sim 4 \text{ K}$) Raman setup that contains a laser with a wavelength of $\lambda = 532 \text{ nm}$, which is focused onto the sample by an $100\times$ objective with a numerical aperture of 0.82. We use a laser intensity of 1 mW and the laser spot diameter is approximately $505 \pm 10 \text{ nm}$ (Supplementary Figure 11). All measurements in this manuscript were performed with linearly polarized light. The reflected and scattered light is detected via a single-mode optical fiber and a spectrometer with a grating of 1200 lines/mm. For performing spatially resolved Raman spectroscopy, our sample is mounted on top of a dc *xy*-piezo stage. The low temperature minimizes the drift during the measurements. We always measure first the Raman spectrum from 250 cm^{-1} up to 1750 cm^{-1} to simultaneously obtain the silicon peak at 521 cm^{-1} and the G peak around 1584 cm^{-1} . We use in-house developed machine learning algorithm to align further Raman maps, which include the 2D peak, with the CD actuator (Supplementary Figure 4).

ASSOCIATED CONTENT

Supporting Information

Details on the fabrication, the capacitive coupling, and the behavior of CD actuators as well as details on the Raman pre-characterization of integrated graphene flakes, the estimation of the Poisson ratio, the measurement reproducibility, the combined spring constant k' , the determination of the laser spot size, and the reported Raman peak shifts due to strain, are available free of charge via the Internet at <http://pucs.acs.org>.

AUTHOR INFORMATION

Corresponding author

E-mail: stampfer@physik.rwth-aachen.de

Notes

The authors declare no competing financial interests.

ACKNOWLEDGMENTS

The authors would like to thank S. Trelenkamp, B. Hermanns, M. Muoth, F. Hassler, F. Haupt for valuable discussions. Support by the ERC (GA-Nr. 280140), the Helmholtz Nanoelectronic Facility (HNF)³² at the Forschungszentrum Jülich, and the Deutsche Forschungsgemeinschaft (DFG) (SPP-1459) are gratefully acknowledged. S.R. acknowledges funding by the National Research Fund (FNR) Luxembourg (project RAM-GRASEA). G.V. acknowledges funding by the Excellence Initiative of the German federal and state governments.

* These two authors contributed equally.

¹ Chen, C.; Rosenblatt, S.; Bolotin, K. I.; Kalb, W.; Kim, P.; Kymissis, I.; Stormer, H. L.; Heinz, T. F.; Hone, J. *Nat. Nanotech.* **2009**, *4*, 861–867.

² Pereira, V. M.; Neto, A. C. *Phys. Rev. Lett.* **2009**, *103*, 046801.

³ Guinea, F.; Katsnelson, M.; Geim, A. *Nat. Phys.* **2010**, *6*, 30–33.

⁴ Verbiest, G.; Brinker, S.; Stampfer, C. *Phys. Rev. B* **2015**, *92*, 075417.

⁵ Fujita, T.; Jalil, M. B. A.; Tan, S. G. *Appl. Phys. Lett.* **2010**, *97*, 043508.

⁶ Grujic, M.; Tadic, M.; Peeters, F. *Phys. Rev. Lett.* **2014**, *113*, 046601.

⁷ Uchoa, B.; Barlas, Y. *Phys. Rev. Lett.* **2013**, *111*, 046604.

⁸ Soodchomshom, B. *Chin. Phys. Lett.* **2013**, *30*, 126201.

⁹ Graf, D.; Molitor, F.; Ensslin, K.; Stampfer, C.; Jungen, A.; Hierold, C.; Wirtz, L. *Nano Lett.* **2007**, *7*, 238242.

¹⁰ Bunch, J. S.; Van Der Zande, A. M.; Verbridge, S. S.; Frank, I. W.; Tanenbaum, D. M.; Parpia, J. M.; Craighead, H. G.; McEuen, P. L. *Science* **2007**, *315*, 490–493.

¹¹ Song, X.; Oksanen, M.; Sillanpää, M. A.; Craighead, H.; Parpia, J.; Hakonen, P. J. *Nano Lett.* **2011**, *12*, 198–202.

¹² Zhang, H.; Huang, J.-W.; Jr., J. V.; Myhro, K.; Maldonado, M.; Tran, D. D.; Zhao, Z.; Wang, F.; Lee, Y.; Liu, G.; Bao, W.; Lau, C. N. *Carbon* **2014**, *69*, 336–341.

¹³ Guan, F.; Kumaravadeivel, P.; Averin, D. V.; Du, X. *Appl. Phys. Lett.* **2015**, *107*, 193102.

¹⁴ Nicholl, R. J.; Conley, H. J.; Lavrik, N. V.; Vlassiouk, I.; Puzyrev, Y. S.; Sreenivas, V. P.; Pantelides, S. T.; Bolotin, K. I. *Nat. Commun.* **2015**, *6*.

⁵ Mohiuddin, T.; Lombardo, A.; Nair, R.; Bonetti, A.; Savini, G.; Jalil, R.; Bonini, N.; Basko, D.; Galotis, C.; Marzari, N. *Phys. Rev. B* **2009**, *79*, 205433.

⁶ Yoon, D.; Son, Y.-W.; Cheong, H. *Phys. Rev. Lett.* **2011**, *106*, 155502.

- ⁹ Huang, M.; Yan, H.; Heinz, T. F.; Hone, J. *Nano Lett.* **2010**, *10*, 4074–4079.
- ¹⁸ For the devices in this work, we find $2\eta = 13.2 \pm 0.5 \text{ nN/V}^2$ (Supplementary Figure 2).
- ¹⁹ Lee, J. E.; Ahn, G.; Shim, J.; Lee, Y. S.; Ryu, S. *Nat. Commun.* **2012**, *3*, 1024.
- ²⁰ Perez Garza, H. H.; Kievit, E. W.; Schneider, G. F.; Staufer, U. *Nano Lett.* **2014**, *14*, 4107–4113.
- ²¹ Downs, C. S. C.; Usher, A.; Martin, J. *J. Appl. Phys.* **2016**, *119*, 194305.
- ²² Neumann, C.; Reichardt, S.; Venezuela, P.; Drögeler, M.; Banszerus, L.; Schmitz, M.; Watanabe, K.; Taniguchi, T.; Mauri, F.; Beschoten, B.; Stampfer, C. *Nat. Commun.* **2015**, *6*, 8429.
- ²³ Banszerus, L.; Janssen, H.; Otto, M.; Epping, A.; Taniguchi, T.; Watanabe, K.; Beschoten, B.; Neumaier, D.; Stampfer, C. *2D Mater.* **2017**, *4*, 025030.
- ²⁴ Novoselov, K. S.; Geim, A. K.; Morozov, S.; Jiang, D.; Zhang, Y.; Dubonos, S.; Grigorieva, I.; Firsov, A. *Science* **2004**, *306*, 666–669.
- ²⁵ Banszerus, L.; Schmitz, M.; Engels, S.; Dauber, J.; Oellers, M.; Haupt, F.; Watanabe, K.; Taniguchi, T.; Beschoten, B.; Stampfer, C. *Science Advances* **2015**, *1*, e1500222.
- ²⁶ Dauber, J.; Sagade, A. A.; Oellers, M.; Watanabe, K.; Taniguchi, T.; Neumaier, D.; Stampfer, C. *Appl. Phys. Lett.* **2015**, *106*, 193501.
- ²⁷ Ma, N.; Zhang, S.; Liu, D. *Physics Letters A* **2016**, *380*, 18841890.
- ²⁸ Goldsche, M.; Khodkov, T.; Kaienburg, P.; Neumann, C.; Trellenkamp, S.; Mussler, G.; Stampfer, C. Low-temperature compatible electrostatic comb-drive actuators with integrated graphene. Nano/Micro Engineered and Molecular Systems (NEMS), 2014 9th IEEE International Conference. 2014; pp 251–255.
- ²⁹ Verbiest, G. J.; Xu, D.; Goldsche, M.; Khodkov, T.; Barzanjeh, S.; von den Driesch, N.; Buca, D.; Stampfer, C. *Appl. Phys. Lett.* **2016**, *109*, 143507.
- ³⁰ Mayorov, A. S.; Gorbachev, R. V.; Morozov, S. V.; Britnell, L.; Jalil, R.; Ponomarenko, L. A.; Blake, P.; Novoselov, K. S.; Watanabe, K.; Taniguchi, T.; Geim, A. *Nano letters* **2011**, *11*, 2396–2399.
- ³¹ Dean, C. R.; Young, A. F.; Meric, I.; Lee, C.; Wang, L.; Sorgenfrei, S.; Watanabe, K.; Taniguchi, T.; Kim, P.; Shepard, K.; Hone, J. *Nat. Nanotech.* **2010**, *5*, 722–726.
- ³² Research Center Jülich GmbH. (2017). HNF - Helmholtz Nano Facility, *Journal of large-scale research facilities* **3**, A112 (2017).

Supporting information: Tailoring mechanically-tunable strain fields in graphene

Supplementary Discussion 1

The effective spring constant k' (see Eq. 1 in the main manuscript) contains the spring constant k_a of the actuator, the spring constant k_P of the (cross-linked) PMMA clamping, and the spring constant k of the graphene flake (see Supplementary Figure 8a). It describes how much of the force $F = \eta V_a^2$ exerted by the actuator is transduced into the graphene sheet. Considering the spring configuration depicted in Supplementary Figure 8a, we find:

$$k' = k \left(1 + k_a \left[\frac{1}{k} + \frac{1}{k_P} \right] \right). \quad (2)$$

It is instructive to see that Eq. 2 reduces to $k' \approx k$ if both following conditions are met: (i) ideal clamping ($k/k_P \ll 1$) and (ii) soft actuator ($k_a/k \ll 1$), which means that all the force exerted by the actuator is directly transduced to the graphene sheet.

We use $k = YW/L$ to estimate the spring constant of a graphene flake of length $L = 2 \mu\text{m}$ and width W . We assume a two-dimensional Young's modulus Y of 362 N/m, as measured by Lee *et al.*¹.

The spring constant k_a of the actuator is estimated from COMSOL simulations² (see for example Supplementary Figure 3). For all CD devices used in this work, we found that k_a is below 15 N/m. Considering the widths of the graphene flakes used in this work (Figure 2d in the main manuscript and Supplementary Figure 9), we find that k is always larger than 500 N/m. Therefore, we conclude that condition (ii) is always fulfilled.

To estimate the ratio k'/k , we use Eq. 1 in the main text to extract k' from fitting $\Delta\omega_{2D}(V_a)$ to our experimental data (see Supplementary Figure 9). Here we use $\partial\omega_{2D}/\partial\epsilon = -83 \text{ cm}^{-1}/\%$. The ratio k'/k , listed in Supplementary Figure 9g, is for all devices larger than 1.8. We point out that this is unlikely explained by a different Young's modulus for the graphene, as it would require a value that is almost twice the literature value (362 N/m). Therefore, we conclude that condition (i) is not met.

Based on this, we can estimate the spring constant of our clamping by inverting Eq. 2 into an equation for k_P :

$$k_P = \frac{k_a}{k'/k - k_a/k - 1}. \quad (3)$$

When considering the clamping geometry (Supplementary Figure 8c,d), we can define a lower and an upper bound for k_P from Euler beam theory. The cross-linked PMMA beams covering the width of the graphene flake give a lower bound for k_P :

$$k_P^{\text{low}} = \frac{16Eb^3h/3}{(W + W_{\text{offset}})^3}, \quad (4)$$

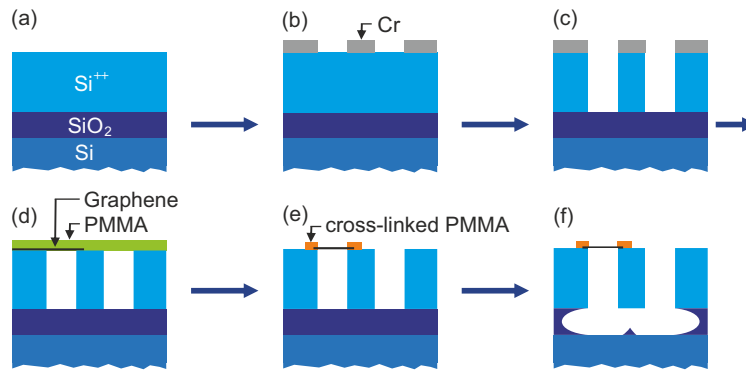
where $E = 4 \text{ GPa}$ is the Young's modulus of cross-linked PMMA^{3,4}, $W_{\text{offset}} = 2 \mu\text{m}$, and b is the width of the cross-linked PMMA beam with thickness h (see Supplementary Figure 8c,d). We included the W_{offset} to account for the effect that a small part of the PMMA beam on the silicon is deformed. We estimated the value of $W_{\text{offset}} \approx 2 \mu\text{m}$ from the scanning electron microscope image in Supplementary Figure 8c,d by the length of the white lines. The beams along the length of the graphene flake give an upper bound for k_P :

$$k_P^{\text{high}} = \frac{Ebh}{L_{\text{overlap}}}, \quad (5)$$

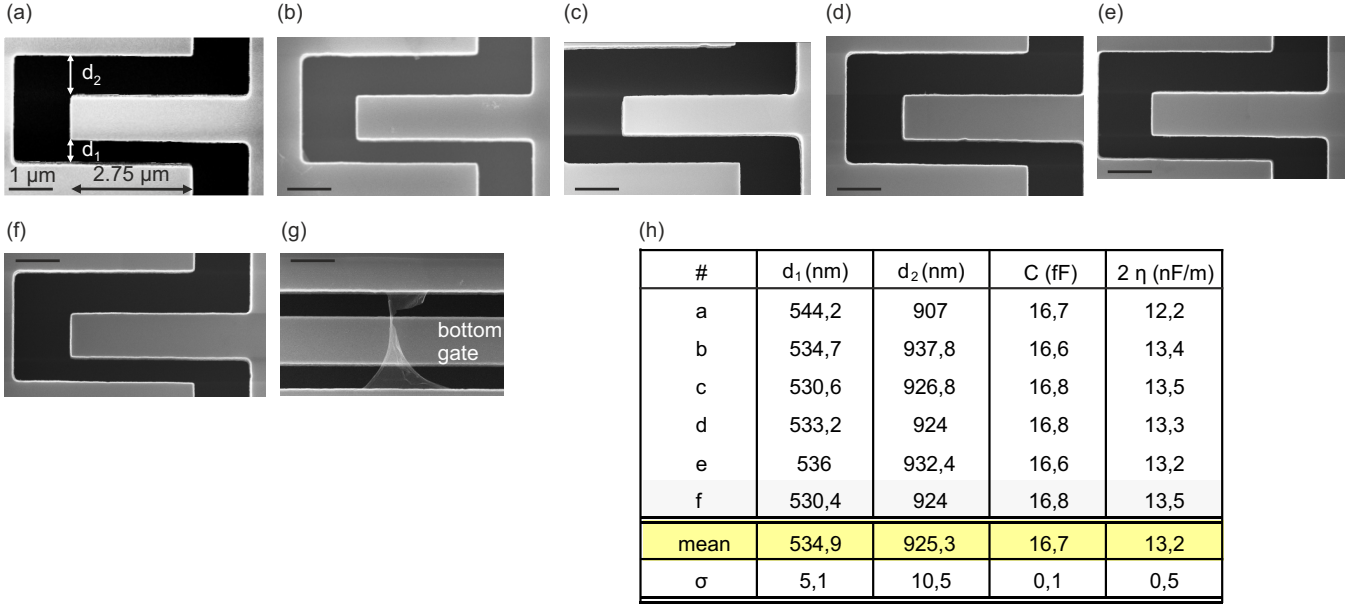
where L_{overlap} is the length of the beam on the graphene (see Supplementary Figure 8c). In this simple picture, we assume a perfect adhesion of the cross-linked PMMA to the silicon and zero adhesion of the graphene to the silicon. In addition, we neglect the fact that the graphene is clamped by multiple beams covering the width of the graphene. Nevertheless, we find that the experimentally extracted k_P is always between the theoretical lower and upper bound (see Supplementary Figure 10). Interestingly, sample number 1 (Supplementary Figure 8d), which is closest to the lower bound, did not have a clamping beam along the length of the graphene (see Supplementary Figure 8c for an example). All the other samples had a beam along the length of the graphene and are therefore closer to the upper bound.

We conclude that the clamping is elastic and acts as a spring in series to k , which are both parallel to the spring of the actuator. The experimentally determined spring constant of the clamping is well within theoretical bounds given by Euler beam theory and the clamping geometry.

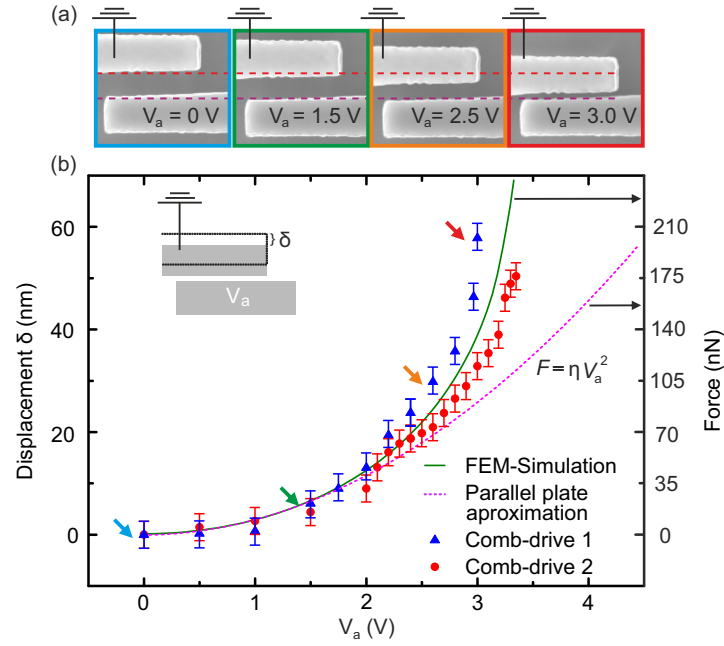
Finally, we point out that $\partial\omega_{2D}/\partial\epsilon = -83 \text{ cm}^{-1}/\%$ will also slightly depend on the crystallographic orientation of the graphene sheet with respect to the pulling direction of the comb-drive. However, this effect is small and therefore cannot explain the observed k'/k ratio.



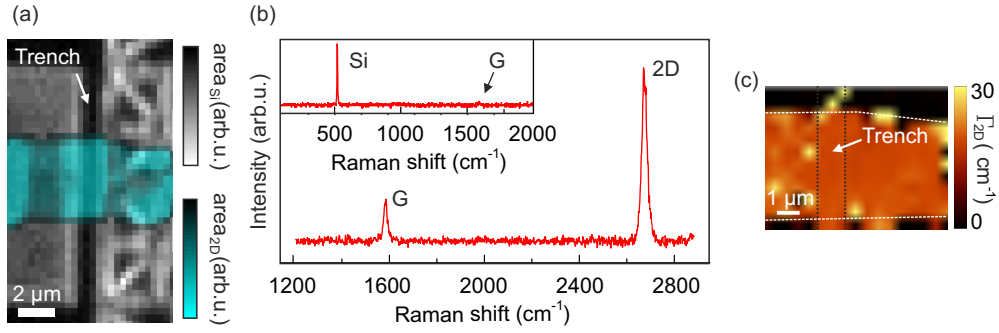
Supplementary Figure 1. Fabrication of comb-drive (CD) actuators with integrated suspended graphene. (a) The CD actuators are fabricated on a silicon on insulator (SOI) substrate that consists from bottom to top of a 500 μm thick Si layer, a 1 μm thick SiO₂ layer, and a 2 μm chemical vapor deposited crystalline, highly p-doped silicon layer. (b) By using standard electron beam lithography techniques, we deposit a Cr hard mask to outline the CD actuator. (c) We pattern the CD actuators via reactive ion etching with C₄F₈ and SF₆. (d) The prepared graphene-PMMA stack is transferred onto the SOI substrate with an accuracy of $\sim 1 \mu\text{m}$. (e) A second electron beam lithography step is used to cross-link the top PMMA layer to clamp the graphene on the CD actuator. The not cross-linked PMMA is dissolved with acetone. (f) To suspend the CD actuator with the integrated suspended graphene, we etch away the SiO₂ layer with a 10% hydrofluoric acid solution and a critical point drying step is used to prevent the CD actuator from collapsing.



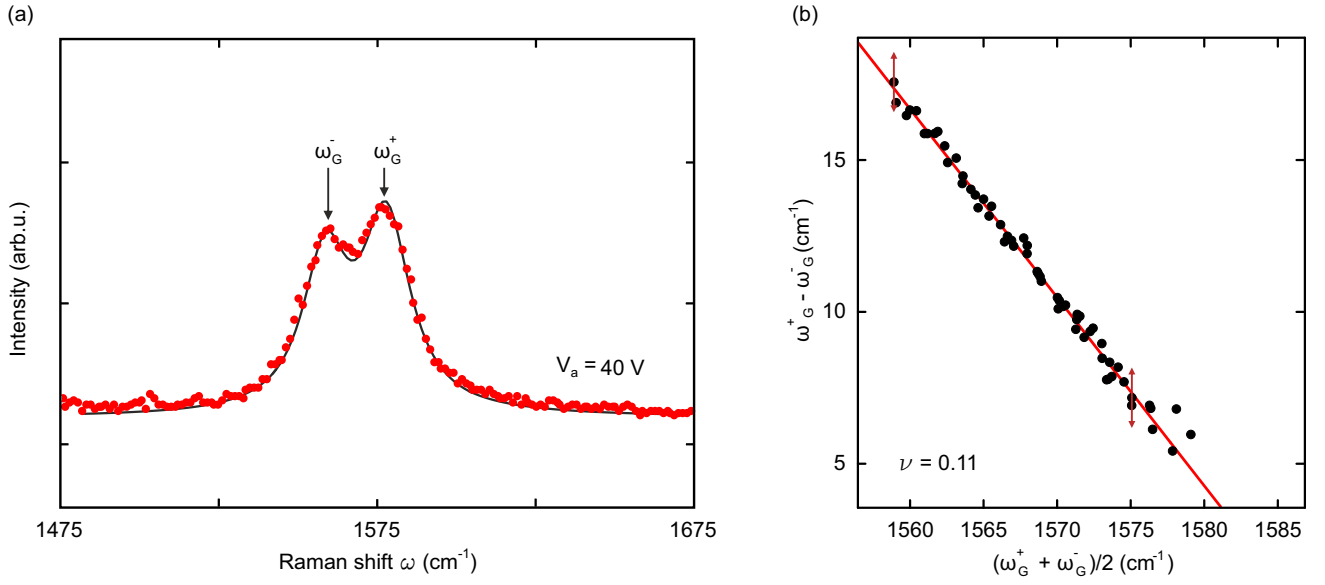
Supplementary Figure 2. Estimation of the capacitive coupling between the interdigitated fingers. We design the distance between the fingers of the CD actuators to be $d_1 = 500$ nm and $d_2 = 900$ nm (see white arrows and labels in panel (a)). To estimate the capacitive coupling between the fingers, we measure these distances for a number of fabricated devices. Panels (a) to (e) show the distances of devices without any graphene and panel (f) shows the distances of a device with integrated graphene as indicated in panel (g). Note that the graphene in panel (g) is suspended over an electrostatic bottom gate that is placed ~ 300 nm underneath the suspended graphene sheet. The scale bars are all $1\ \mu\text{m}$ long. All measured distances are listed in panel (h). We find that all distances are slightly higher than designed. Note that the distances extracted from the device with integrated graphene is no different from the ones measured on devices without graphene. Using the finger overlap area A as well as the number of fingers $N = 118$, we find a capacitance $C = \epsilon_0 AN(d_1^{-1} + d_2^{-1})$ of around 16.7 ± 0.1 fF between the fingers. The capacitive coupling $2\eta = \epsilon_0 AN(-d_1^{-2} + d_2^{-2})$ relevant for the electrostatic force (see main manuscript) is therefore 13.2 ± 0.5 nF/m (or $2\eta = 13.2 \pm 0.5 \text{ nN/V}^2$).



Supplementary Figure 3. Scanning electron microscope (SEM) characterization of empty CD actuators. (a) SEM images of the separation between the interdigitated fingers of an empty CD actuator (without a graphene flake) as a function of applied potential V_a . (b) The displacement δ (see inset) of two different CD actuators extracted from SEM images for increasing V_a . The arrows indicate the corresponding SEM image in panel (a). The displacement δ shows a nearly quadratic dependence on applied potential V_a , which is consistent with the electrostatic force. To estimate this force, we performed COMSOL simulations with the fabricated device geometry². The extracted spring constant of the CD actuator from the simulations is $\approx 3.5\text{ N/m}$. The green line depicts the simulation result and indicates a maximum force of $\approx 200\text{ nN}$ at a displacement of 60 nm . The pink line shows that the force obtained using the parallel plate approximation for the capacitance is in good agreement with the simulation for displacements up to 10 nm . Please note that $2\eta = 8.7 \pm 0.5\text{ nF/m}$ for these devices, as they had a slightly different design than the devices shown in Supplementary Figure 2.



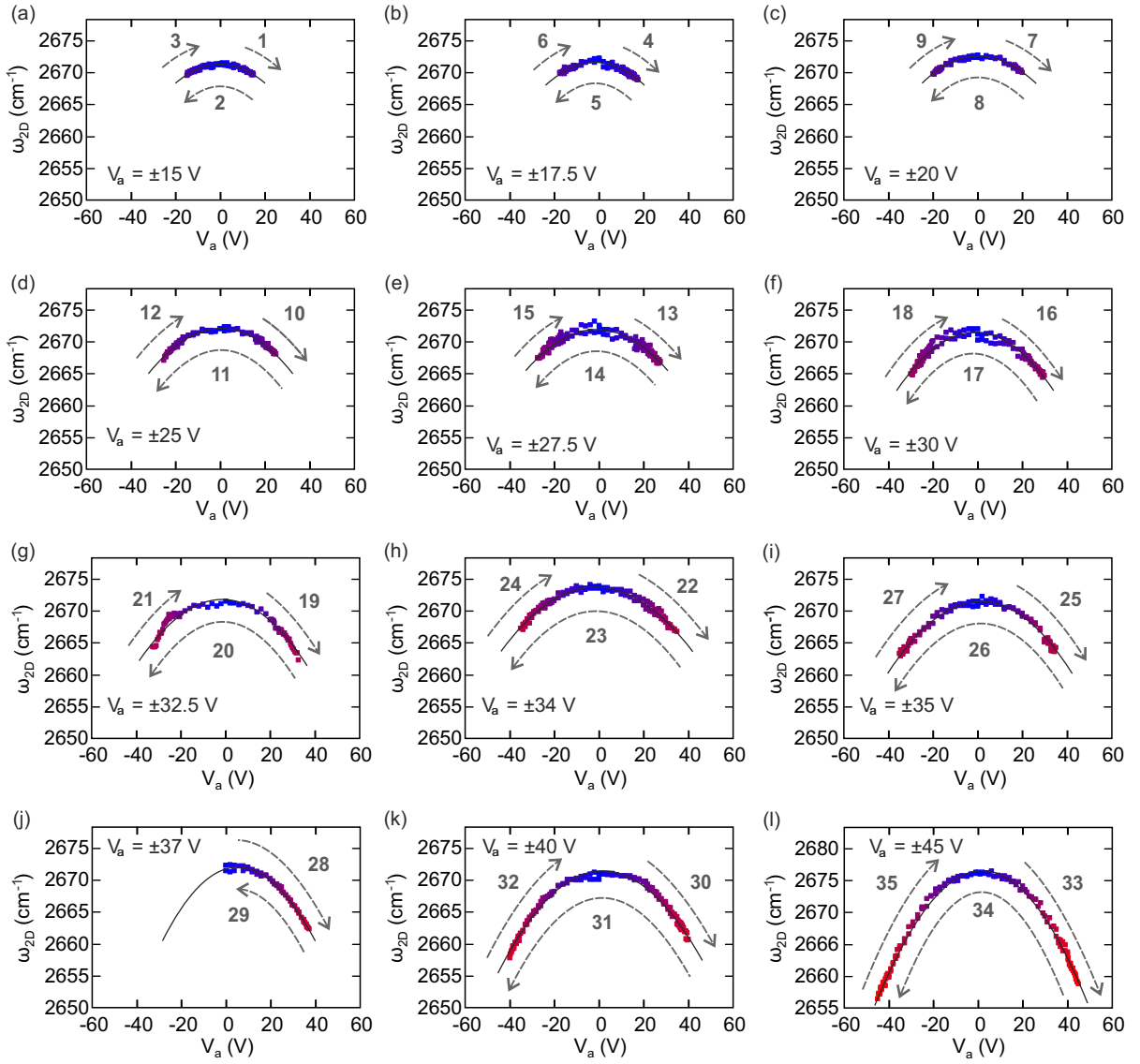
Supplementary Figure 4. Raman pre-characterization. (a) Raman map of the silicon peak area at 521 cm^{-1} superimposed with a Raman map of the 2D peak area, which has been obtained as follows. In a first Raman map, we measure from 250 cm^{-1} to 1750 cm^{-1} , which gives us both the silicon peak and the G peak of the graphene. In a second Raman map, we measure both the G and 2D peak. By aligning both measured Raman maps of the G peak, we can superimpose the 2D peak with the silicon peak. (b) Typical Raman spectrum of a suspended graphene flake, which was transferred on one of our CD actuators. Apart from the visible G and 2D peak, it is important to note the absence of a D peak (expected around 1345 cm^{-1}). The inset shows the Raman spectrum around the silicon peak at 521 cm^{-1} that is obtained on a CD actuator. (c) The Raman map of the width Γ_{2D} of the 2D peak obtained on a typical sample.



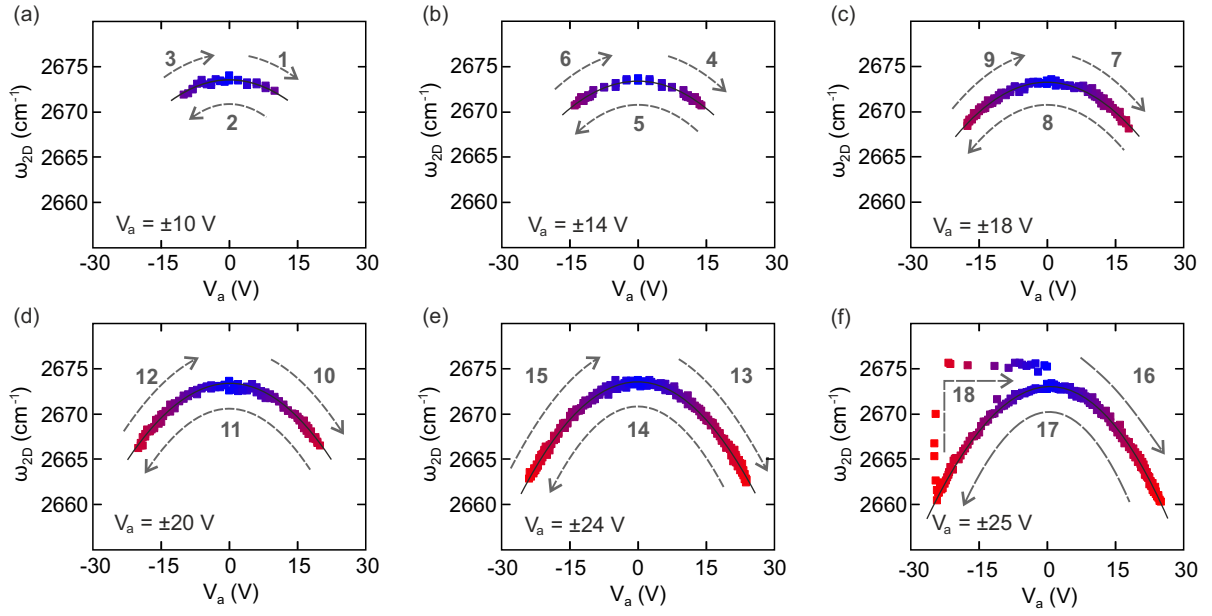
Supplementary Figure 5. Estimation of the Poisson ratio. (a) The Raman spectrum of the G peak for $V_a = 40$ V shows a splitting into two peaks due to uniaxial strain as depicted in Figure 1e of the main manuscript. These peaks are the so-called ω_G^- and ω_G^+ peak at lower and higher Raman shift, respectively⁵. (b) The frequency difference $\omega_G^+ - \omega_G^-$ as a function of their average $(\omega_G^+ + \omega_G^-)/2$ allows us to extract the Poisson ratio of the suspended graphene sheet according to the following equation⁵:

$$\omega_G^+ - \omega_G^- = -\frac{0.99}{1.99} \frac{1 + \nu}{1 - \nu} \left(\frac{\omega_G^+ + \omega_G^-}{2} - \omega_G^0 \right),$$

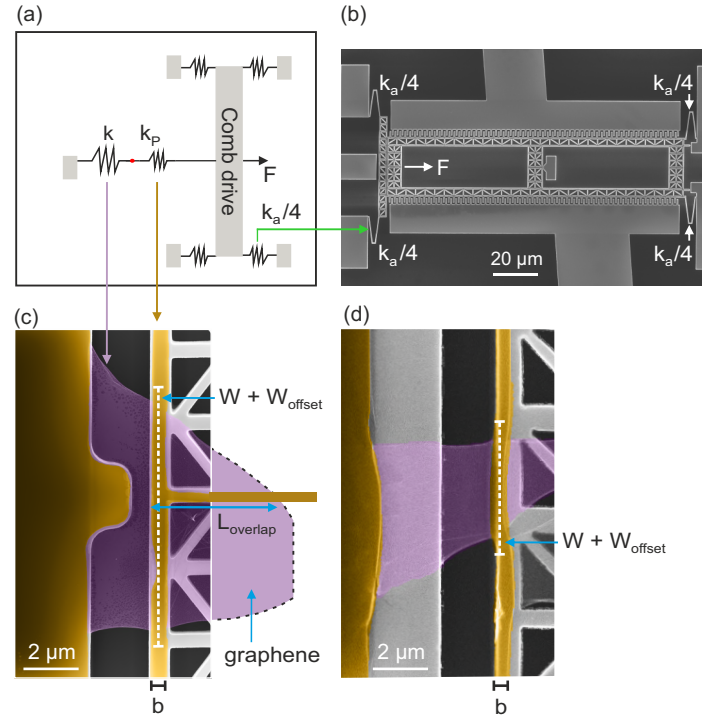
where ν is the Poisson ratio and ω_G^0 is the ω_G frequency at zero strain. By fitting our data between the vertical arrows with a linear function (see red line), we obtain a Poisson ratio of $\nu = 0.11$. The extracted Poisson ratio is in good agreement with the one reported in the literature for graphite and suspended graphene ($\nu = 0.13$)⁵.



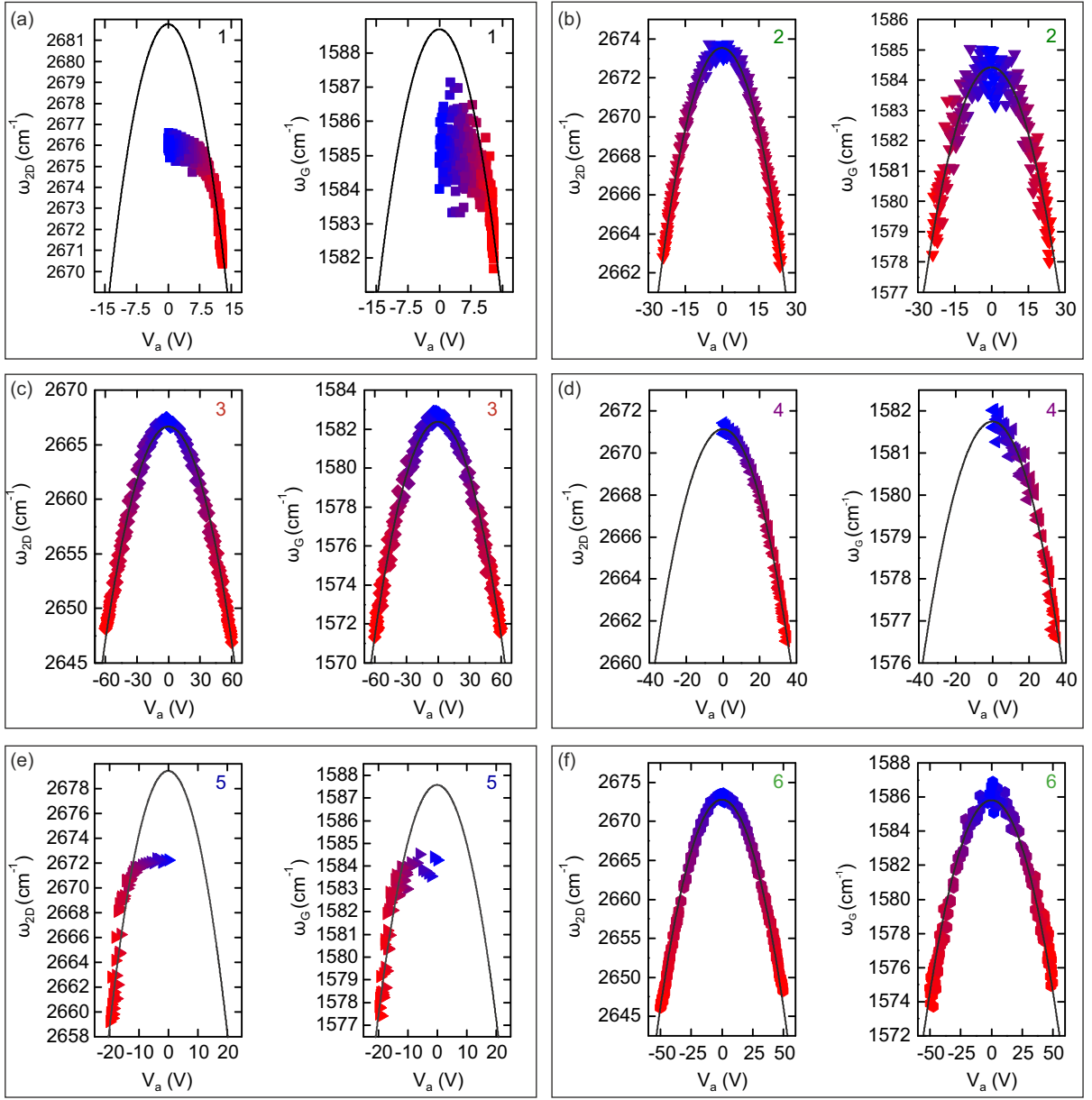
Supplementary Figure 6. Measurement reproducibility. We show the extracted ω_{2D} frequency obtained on the same position of the graphene flake for different measurement cycles. The measurements are depicted in chronological order from panel (a) to (l). In each cycle, we sweep the potential V_a back and forth (gray arrows) while monitoring the Raman spectra. After each cycle, we increase the maximum applied $|V_a|$ and start a new cycle. We observe no hysteresis and hence no noticeable slipping of the clamped graphene. Hence, we can combine all cycles into a single graph as was done in Figure 2 of the main manuscript. This allows us to obtain an unprecedented amount of data points on each sample. Note that the scale in panel (l) is different from those in (a)-(k). After measuring panel (k), we moved the sample into a different measurement system, which resulted in an overall shift of ω_{2D} . Surprisingly, the tuning with V_a did not change at all indicating the mechanical stability of our samples.



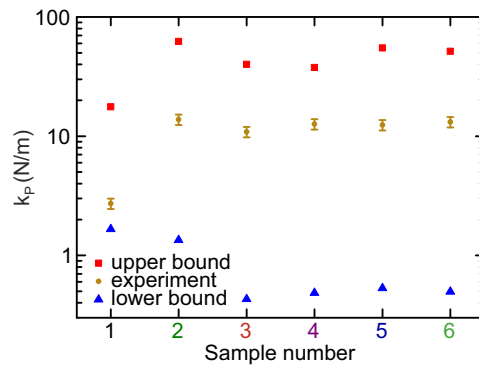
Supplementary Figure 7. Measurement reproducibility. We show the extracted ω_{2D} frequency obtained on the same position of the graphene flake for different measurement cycles. The measurements are depicted in chronological order from panel (a) to (f). In each cycle, we sweep the potential V_a back and forth (gray arrows) while monitoring the Raman spectra. After each cycle, we increase the maximum applied $|V_a|$ and start a new cycle. By increasing $|V_a|$ to 25 V, we observe the rupturing of the graphene flake (see Figure 2c in the main text).



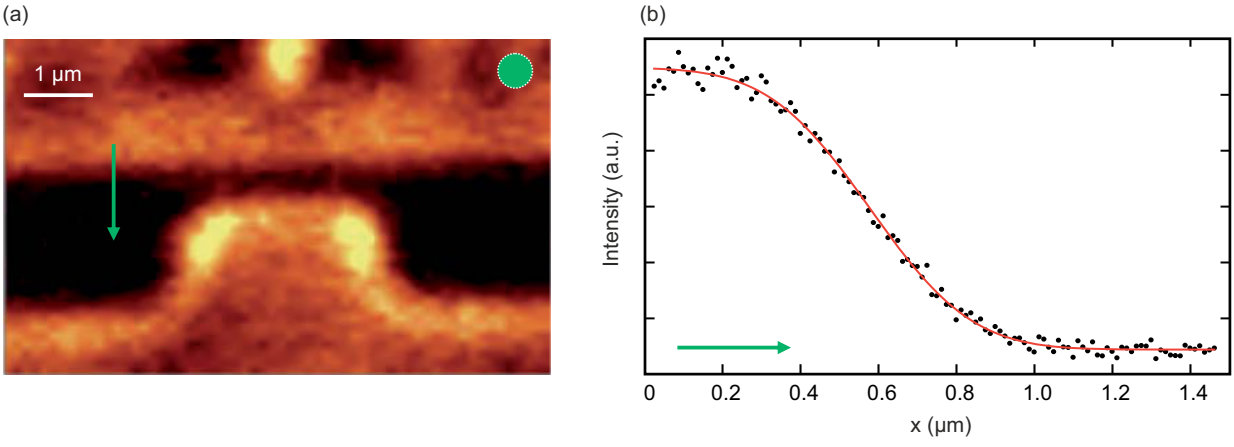
Supplementary Figure 8. Spring configuration of the devices. (a) Schematic illustration of the springs in our measured samples. (b) The green arrow indicates the spring k_a of the actuator. (c) The purple arrow indicates the spring k of the graphene sheet and the dark yellow arrow indicates the spring k_p of the clamping. The clamping consists of cross-linked PMMA beams along the width of the graphene flake as well as a beam along the length of the graphene flake on the actuator. (d) The clamping geometry of sample 1 in the main manuscript does not have the beam with length L_{overlap} along along the length of the graphene flake on the actuator. To fully illustrate the length L_{overlap} , we drew, as a guide to the eye, the outline of the graphene flake beyond the SEM image. The white dashed lines in panels (c) and (d) indicate the part of the clamping on the silicon that is also deformed together with the graphene flake of width W (see Supplementary Discussion 1). The length of the white dashed lines is equal to $W + W_{\text{offset}}$. The black lines in panels (c) and (d) indicate the width b of the cross-linked PMMA beam.



Supplementary Figure 9. Estimation of the relative $\omega_{2D(G)}$ shift per unit strain. Panels (a) to (f) show the Raman 2D and G peak frequencies ω_{2D} and ω_G as function of the potential V_a for six different samples. The colour of the sample numbers correspond to the one of the slope in Figure 2b of the main manuscript. Samples 1 and 5 are the only ones to show slack. The parabolic behavior agrees with the electrostatic force $F = \eta V_a^2$. (g) We find from fitting our data with $\Delta\omega_{2D(G)} = P_{2D(G)} V_a^2$ (see parabolas in panels (a)-(f)) and using $\partial\omega_{2D}/\partial\epsilon = -83 \text{ cm}^{-1}/\%$, the measured length $L = 2 \text{ μm}$ and individual width W as well as the estimated $k = Y_{2D}W/L$ with $Y_{2D} = 362 \text{ N/m}^1$, the ratio k'/k . As $k'/k > 1$, we must have an effective spring k' that is different from the one for pristine graphene.



Supplementary Figure 10. Spring constant estimation of the clamping. The extracted spring constant k_P of the clamping for each different sample lies well within the bounds given by Euler-beam theory (see Supplementary Discussion 1). The colour of the sample numbers correspond to the one of the slope in Figure 2b of the main manuscript. We conclude that the clamping is elastic and acts as a spring in series to the spring k of the graphene flake, which are both parallel to the spring k_a of the actuator.



Supplementary Figure 11. Determination of the laser spot size. (a) Raman map of the silicon peak intensity at 521 cm^{-1} of a CD actuator without a graphene flake. (b) Intensity of the silicon peak along the green arrow in panel (a). As the edge of the CD actuator is well defined and sharp (see e.g. SEM images in Supplementary Figure 2), we can understand the measured intensity profile as a convolution of a step function with a Gaussian function. Therefore, we can determine the laser spot size by fitting the intensity with $I(x) = I_0 \text{erf}\left(\frac{\sqrt{2}(x-x_0)}{r}\right)$, in which r is the radius of the Gaussian profile and x_0 is the position of the edge. The fit result, shown in red, gives us a x_0 of $554 \pm 4 \text{ nm}$ and a beam diameter of $505 \pm 10 \text{ nm}$.

Author		$\frac{\partial\omega_G}{\partial\epsilon}$ (cm ⁻¹ /%)	$\frac{\partial\omega_{2D}}{\partial\epsilon}$ (cm ⁻¹ /%)
Mohiuddin <i>et al.</i> ⁵	supported	-21.25	-64
Mohiuddin <i>et al.</i> ⁵	suspended	-27.5	-83
Yoon <i>et al.</i> ⁶	supported	-23.95	A: -53.1 Z: -46.9
Frank <i>et al.</i> ⁷	supported	-20.5	-56.65
Polyzos <i>et al.</i> ⁸	suspended	-28	-89
Huang <i>et al.</i> ⁹	supported	-9.05	A: -26.1 Z: -23
Ni <i>et al.</i> ¹⁰	supported	-14.2	-27.8

Supplementary Table 1. Summary of published Raman peak shifts due to strain. If strain was applied along the armchair and zigzag direction, this is denoted with A and Z, respectively. The reported values for $\frac{\partial\omega_G}{\partial\epsilon}$ and $\frac{\partial\omega_{2D}}{\partial\epsilon}$ show a large spread, which can be attributed to how strain was applied to the graphene flake. All studies in this table used a bendable substrate except for Polyzos *et al.*⁸. This has two important consequences: (i) graphene does not exhibit its intrinsic Poisson ratio and (ii) the strain is possibly not properly transferred into the graphene flake due to the large difference between Young's modulus of the substrate and the graphene flake¹¹. The latter leads to an overestimation of the induced strain and thus to an underestimation of $\frac{\partial\omega_G}{\partial\epsilon}$ and $\frac{\partial\omega_{2D}}{\partial\epsilon}$. Therefore, we base our strain estimations on the conservative value of $\frac{\partial\omega_{2D}}{\partial\epsilon} = -83$ cm⁻¹/% reported by Mohiuddin *et al.*⁵ and Polyzos *et al.*⁸, which is also agreeing with theory⁵.

-
- * These two authors contributed equally.
- ¹ Lee, C., Wei, X., Kysar, J. W. & Hone, J. Measurement of the elastic properties and intrinsic strength of monolayer graphene. *Science* **321**, 385 (2008).
 - ² www.comsol.com.
 - ³ Teh, W. H., Liang, C.-T., Graham, M. & Smith, C. G. Cross-linked pmma as a low-dimensional dielectric sacrificial layer. *J. Microelectromech. Syst.* **12**, 641 (2003).
 - ⁴ Torres, J. M., Stafford, C. M. & Vogt, B. D. Manipulation of the elastic modulus of polymers at the nanoscale: Influence of uv-ozone cross-linking and plasticizer. *ACS Nano* **4**, 5357 (2010).
 - ⁵ Mohiuddin, T. *et al.* Uniaxial strain in graphene by raman spectroscopy: G peak splitting, grüneisen parameters, and sample orientation. *Phys. Rev. B* **79**, 205433 (2009).
 - ⁶ Yoon, D., Son, Y.-W. & Cheong, H. Strain-dependent splitting of the double-resonance raman scattering band in graphene. *Phys. Rev. Lett.* **106**, 155502 (2011).
 - ⁷ Frank, O. *et al.* Raman 2D-band splitting in graphene: theory and experiment. *ACS Nano* **5**, 2231 (2011).
 - ⁸ Polyzos, I. *et al.* Suspended monolayer graphene under true uniaxial deformation. *Nanoscale* **7**, 13033 (2015).
 - ⁹ Huang, M., Yan, H., Heinz, T. F. & Hone, J. Probing strain-induced electronic structure change in graphene by raman spectroscopy. *Nano Lett.* **10**, 4074 (2010).
 - ¹⁰ Ni, Z. H. *et al.* Uniaxial strain on graphene: Raman spectroscopy study and band-gap opening. *ACS Nano* **2**, 2301 (2008).
 - ¹¹ Liu, Z. *et al.* Strain and structure heterogeneity in MoS₂ atomic layers grown by chemical vapour deposition. *Nat. Commun.* **5**, 5246 (2014).